Development of a Prototype Atomic Clock Based on Coherent Population Trapping

A thesis submitted in partial fulfillment of the requirement
for the degree of Bachelor of Science
Physics from the College of William and Mary in Virginia,

by

Nathan T. Belcher

Accepted for: BS in Physics

Advisor: I. Novikova

W. J. Kossler

Williamsburg, Virginia
May 2008

Abstract

The goal of this project is to construct a prototype atomic clock using coherent population trapping (CPT) in a rubidium vapor cell. We have created a laser system to lock the laser's frequency to an atomic resonance in rubidium and utilized radiofrequency (rf) modulation to create a sideband and carrier comb. With the system assembled, we have observed CPT and locked the CPT to our rf source to create a prototype atomic clock. In the future, we will continue to study the CPT resonances to make the clock better.

1 Introduction

In the last decade, advances have been made in creating miniature (sub-cubic centimeter) atomic clocks, based on laser probing of an atomic vapor. The laser employed in these clocks is a vertical-cavity surface-emitting laser (VCSEL), which has useful characteristics for this application: low power consumption, ease of current modulation with radiofrequency (rf) signals, and use in minature atomic clocks.

The atomic clocks contain three parts: a hyperfine transition (in the microwave region) between two long-lived spin states of an alkali metal (that has a hydrogen-like spectrum), a frequency modulator with counter, and a laser. The element of use in this atomic clock is rubidium, which is an alkali metal. The frequency modulator provides phase modulation, creating two electro-magnetic fields at different frequencies out of one physical laser. A counter matches the frequency driven by the modulator to give a reference for time, and the laser drives the entire process. To keep the laser at a set frequency corresponding to the atomic transition, another part called a dichroic atomic vapor laser locking (DAVLL) system is needed. The DAVLL uses an error signal determined by the difference of signal in two photodetectors to keep the laser's frequency on a rubidium resonance. In addition, electronics of the frequency modulator keep the modulation frequency at the "clock" frequency, allowing an atomic clock to be created for an extended period of time.

The overall goal of this project is to create a prototype atomic clock, which we have done successfully. This paper describes the following: theories underlying the atomic clock in section 2; the experimental setup in section 3; creating and measuring coherent population trapping (CPT) in section 4; creating and measuring the clock in section 5; further CPT studies in section 6.

2 Theory

2.1 Coherent Population Trapping

Coherent population trapping (CPT) drives the clock, so it is important to understand the underlying theory. We will begin with the theory of a two-level system, and then move to a three-level system. The treatment of this theory will be semiclassical, with the atoms treated as quantum objects in a classical electromagnetic field. For the

two-level system, most of the underlying mathematics will be omitted, and only the equations needed to describe the three-level system will be introduced.

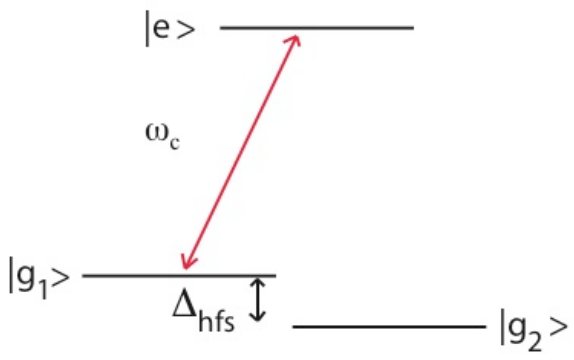

Figure 1: A two-level system. Level g_1 is a state in $5S_{1/2}$, and level e is the excited state 794.7 nm away from the $5S_{1/2}$ state. The level g_2 is included to compare with the Λ system.

We first begin with figure 1, where the electromagnetic field interacts with a two-level atom. In this case, the Schrödinger equation to find the wavefunction of the unpaired electron in a rubidium atom in the electromagnetic field is:

$$i\hbar\dot{\psi}(t) = (\hat{H}_0 + \hat{H}_{int})\psi \tag{1}$$

The first term $\hat{H}_0$ is the atomic part of the Hamiltonian, and represents the electronic energy levels in the field of the nuclei. The second term describes the interaction of an atom with the electromagnetic field, and can be defined as:

$$\hat{H}_{int} = -e\hat{\vec{E}} \cdot \hat{\vec{r}} = -e\hat{E}\hat{x} \tag{2}$$

The wavefunction ψ is defined for the two-level interaction as:

$$|\psi(t)\rangle = \alpha(t)\,|e\rangle + \beta(t)\,|g\rangle\,, \tag{3}$$

and it is convenient to write the Hamiltonian operators in the bases of the states $|e\rangle$ and $|g\rangle$. Following the definition for the matrix elements for the electron dipole moments we have:

$$\hat{H}_0 = \hbar\omega_e\,|e\rangle\langle e| + \hbar\omega_g\,|g\rangle\langle g| \tag{4}$$

$$\hat{H}_{int} = \wp_{eg}(E\,|e\rangle\langle g| + E^*\,|g\rangle\langle e|) \tag{5}$$

where

$$\langle g| - e\cdot x|e\rangle = \langle e| - e\cdot x|g\rangle = \wp_{eg} \tag{6}$$

$$\langle g| - e\cdot x|g\rangle = \langle e| - e\cdot x|e\rangle = 0 \tag{7}$$

The energies of the ground and excited states are $\hbar\omega_g$ and $\hbar\omega_e$, respectively, and it is convenient to set the energy of the ground state as a zero level ($\omega_g = 0$). We then define $\omega_{eg} = \omega_e - \omega_g$ as the frequency of atomic transition.

We next write down the expression for the electric field of a monochromatic electromagnetic wave and make some simplifications, arriving at equations for α and β. By solving these equations for a constant amplitude of the electromagnetic field and resonant interaction, the equation for α(t) becomes that of a harmonic oscillator

$$\ddot{\tilde{\alpha}} = -\frac{\wp_{eg}\mathcal{E}^2}{2\hbar}\,\tilde{\alpha}, \tag{8}$$

where $\mathcal{E}$ is the amplitude of a monochromatic electromagnetic wave. The atomic population $|\alpha|^2$ oscillates between the ground and excited states with a frequency:

$$\Omega = \frac{\wp_{eg}\mathcal{E}}{\hbar} \tag{9}$$

This effect is known as Rabi oscillations, and frequency Ω is called the Rabi frequency. To find $\ddot{\tilde{\alpha}}$, we use a technique known as the rotating wave approximation. Two approximations are made: one to neglect fast oscillating terms due to a weak electromagnetic field; another to assume that the electromagnetic field's frequency is near the resonant frequency.

While the calculations up to this point are correct theorectically, they are somewhat incomplete without taking into account any decoherence mechanisms. The most fundamental decoherence mechanism for a two-level system is spontaneous emission, caused by the interaction of atoms with vacuum fluctuations. Spontaneous emission limits the time an atom can spend in the excited state. By adding a relaxation term Γ to the excited state amplitude, we can represent the loss of atoms in the excited state. This term is added in the equations

$$\dot{\tilde{\alpha}} = -(\frac{\Gamma}{2} + i\Delta)\tilde{\alpha} + \frac{i\Omega}{2}\beta \tag{10}$$

$$\dot{\beta} = \frac{\Gamma}{2} + \frac{i\Omega^*}{2}\alpha \tag{11}$$

where $\Delta = \omega_{eg} - \omega$ is the difference between the frequency of the atomic transition and the laser frequency. This term is also often referred to as the detuning of the laser from the atomic transition.

For simplicity, we assume that the total population of both levels is always 1. We use the normalization condition of $\alpha^*\alpha + \beta^*\beta = 1$ to find

$$\tilde{\alpha} = \frac{i\Omega}{\sqrt{\Gamma^2 + |\Omega|^2 + 4\Delta^2}} \tag{12}$$

$$\beta = \frac{\Gamma + 2i\Delta}{\sqrt{\Gamma^2 + |\Omega|^2 + 4\Delta^2}} \tag{13}$$

From these equations, we can see how the populations of the excited and ground states $|\alpha|^2$ and $|\beta|^2$ depend on the strength of the electromagnetic field. If the applied

field is weak ($\Omega \ll \Gamma$), then most of the atomic population is in the ground state and only a small fraction of atoms $\propto |\Omega/\Gamma|^2$ is excited.

We can next write the expression for the polarization of the medium in the following form

$$\mathcal{P} = iN\wp_{eg}\Omega\frac{\Gamma - 2i\Delta}{\Gamma^2 + 4\Delta^2 + |\Omega|^2}, \tag{14}$$

and define the susceptibility of an atomic medium as a ratio between the applied electric field and induced polarization as

$$\mathcal{P} = \varepsilon_0\chi\mathcal{E} \tag{15}$$

Plugging in equation (14) into the previous equation, we find

$$\chi(\Delta) = i\frac{n_{Rb}\wp_{eg}^2}{\varepsilon_0\hbar}\frac{\Gamma - 2i\Delta}{\Gamma^2 + 4\Delta^2 + |\Omega|^2} \tag{16}$$

where n_{Rb} is the number density of Rb atoms in the vapor. The real part of the susceptibility gives an expression for the refractive index, and the imaginary part describes the absorption coefficient

$$\eta(\Delta) = kIm[\chi(\Delta)] = \frac{2\pi N\wp_{eg}^2}{\varepsilon_0\hbar\lambda}\frac{\Gamma}{\Gamma^2 + 4\Delta^2 + |\Omega|^2} \tag{17}$$

The absorption on the electromagnetic field in the two-level system gives an absorption resonance with the width corresponding to the decay rate Γ of the excited state $|\alpha\rangle$. This value is a few MHz in stationary atoms, and a few hundred MHz in a thermal vapor cell.

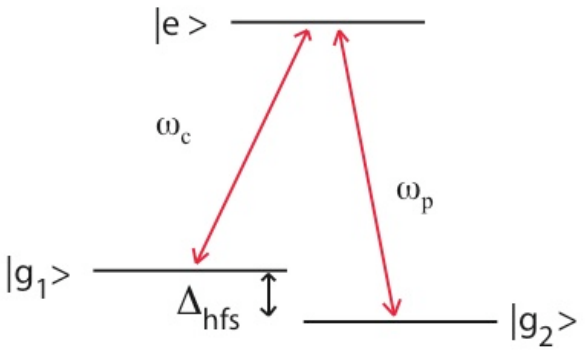

Figure 2: A Λ system. Levels g_1 and g_2 are states in $5S_{1/2}$ separated by the hyperfine splitting (6.834 GHz), and level e is 794.7 nm away from the $5S_{1/2}$ state.

To move to a three-level system (known as a Λ system), we simply join two two-level systems. As seen in figure 2, the three-level system consists of two ground states

$|g_1\rangle$ and $|g_2\rangle$ separated by an energy $\hbar\Delta_{hfs}$ and a single excited state $|e\rangle$. Δ_{hfs} is the frequency of the hyperfine splitting between the two ground states. The atomic and interaction Hamilitonians for this system are:

$$\hat{H} = \hbar\omega_e |e\rangle\langle e| + \hbar\omega_{g_2} |g_2\rangle\langle g_2| + \hbar\omega_{g_1} |g_1\rangle\langle g_1| \tag{18}$$

$$\hat{H}_{int} = \wp_{eg}(E_1 |e\rangle\langle g_1| + E_1^* |g_1\rangle\langle e| + E_2 |e\rangle\langle g_2| + E_2^* |g_2\rangle\langle e| \tag{19}$$

For each of the electromagnetic fields E_1 (contains the frequency ω_c) and E_2 (contains the frequency ω_p), we can calculate the respective Rabi frequencies from the methods established earlier in this section. We find:

$$\Omega_1 = \frac{\wp_{eg_1}\mathcal{E}_1}{\hbar} \tag{20}$$

$$\Omega_2 = \frac{\wp_{eg_2}\mathcal{E}_2}{\hbar} \tag{21}$$

After making some definitions and finding the eigenvalues of the Hamiltonian with an eigenstate ψ, we calculate the dark state for a three-level system. This wavefunction is known as the dark state because atoms in it will not absorb either electromagnetic field, giving almost 100 percent transmission through the atoms such that $H_{int}|dark\rangle = 0$. The equation is:

$$|dark\rangle = \frac{\Omega_1 |g_2\rangle - \Omega_2 |g_1\rangle}{\sqrt{|\Omega_1|^2 + |\Omega_2|^2}} \tag{22}$$

where Ω_1 and Ω_2 are the Rabi frequencies of the two transitions.

To calculate the susceptibility of the three-level system, a density matrix must be used. We will not describe this here, but will state the result of this mathematical treatment [4]:

$$\chi(\Delta) = i\frac{n_{Rb}\wp_{eg}^2}{\varepsilon_0\hbar}\frac{(\Gamma_{dark} + i\Delta)}{\Gamma(\Gamma_{dark} + i\Delta) + \Omega^2/4} \tag{23}$$

where Γ_{dark} is the decay rate of the dark state. Again, the real part of the susceptibility gives an expression for the refractive index, and the imaginary part describes the absorption coeffiecient

$$\eta(\Delta) = kIm[\chi(\Delta)] = \frac{n_{Rb}\wp_{eg}^2}{\varepsilon_0\hbar}\frac{\Delta^2\Gamma - \Gamma_{dark}(\Delta^2 - \Gamma\Gamma_{dark} - \Omega^2/4)}{(\Delta^2 - \Gamma\Gamma_{dark} - \Omega^2/4)^2 + \Delta^2\Gamma^2} \tag{24}$$

When on resonance, $\eta \propto \Gamma_{dark}$. Since Γ_{dark} represents the relaxation rate of the forbidden transtion between the two ground states, it can be very small. This makes the absorption also very small, giving a very narrow transmission peak for two-photon detuning.

For a simple symmetric three-level model ($\Omega_1 = \Omega_2 = \Omega$) [5], the shape and height of the coherent population trapping can be determined from analytical calculations. For a single atom at rest in the case of resonant, low-intensity electromagnetic fields, the resonance will be Lorentzian with a width

$$\gamma_{CPT} = 2\Gamma_{dark} + \frac{\Omega^2}{\Gamma} \tag{25}$$

that depends on the relaxation rates of the ground- and excited-state coherence, Γ_{12} and Γ, respectively. In the same low-intensity limit, the height of the resonance H is given by the number of atoms populating the dark state

$$H \propto n_{Rb} \frac{\Omega^4}{\Gamma^3} \frac{1}{2\Gamma_{dark} + \Omega^2/\Gamma} \tag{26}$$

where n_{Rb} is the number density of Rb atoms in the vapor.

2.2 Phase Modulation

EIT is very sensitive to frequency difference between two laser fields in the Λ system, so a few problems exist. The first problem is the laser will move around a set frequency in a random way ("jump"), regardless of the quality of the laser. If two physically separate lasers are used at two different frequencies, they will both jump randomly and not have any correlation. To correct this problem, two lasers can be created out of one physical laser by modulating its phase. The relative frequency of the two fields can be set by an external generator, and this creates a carrier with sideband comb. Even though there will still be jumps around the set frequency, both laser fields will jump in the same way.

The mathematics behind phase modulation is useful. A generic electromagnetic wave described by the following equation

$$E = E_0 e^{ikx - i\omega t + i\varphi(t)} \tag{27}$$

where E_0 is the amplitude of the wave, ω is the phase, and k is a vector that points in the direction the wave is traveling. Phase φ(t) is the modulated in the form

$$\varphi(t) = \varepsilon sin(\omega_m t) \tag{28}$$

where ε is the amplitude of modulation and ω_m is the modulation frequency. Taking a Bessel function decomposition of φ into E gives the final result of:

$$E = \sum_{n=0}^{\infty} E_0 J_n(\varepsilon) e^{ikx - i(\omega - n\omega_m)t} \tag{29}$$

This equation is the basis for the carrier and sideband comb, because the frequency difference between the carrier and each nth sideband is determined by $\omega - n\omega_m$.

An advantage of using the VCSELs is that their output can be phase-modulated by direct current modulation up to relatively high (10 GHz) frequencies. In addition, phase modulation allows matching of the hyperfine splitting in the rubidium vapor at 6.834 GHz.

3 Experiment

In the experimental setup, there are four main parts: laser system, rubidium cell and shields, DAVLL (optical laser lock), and oscillator. From these parts, we are able to

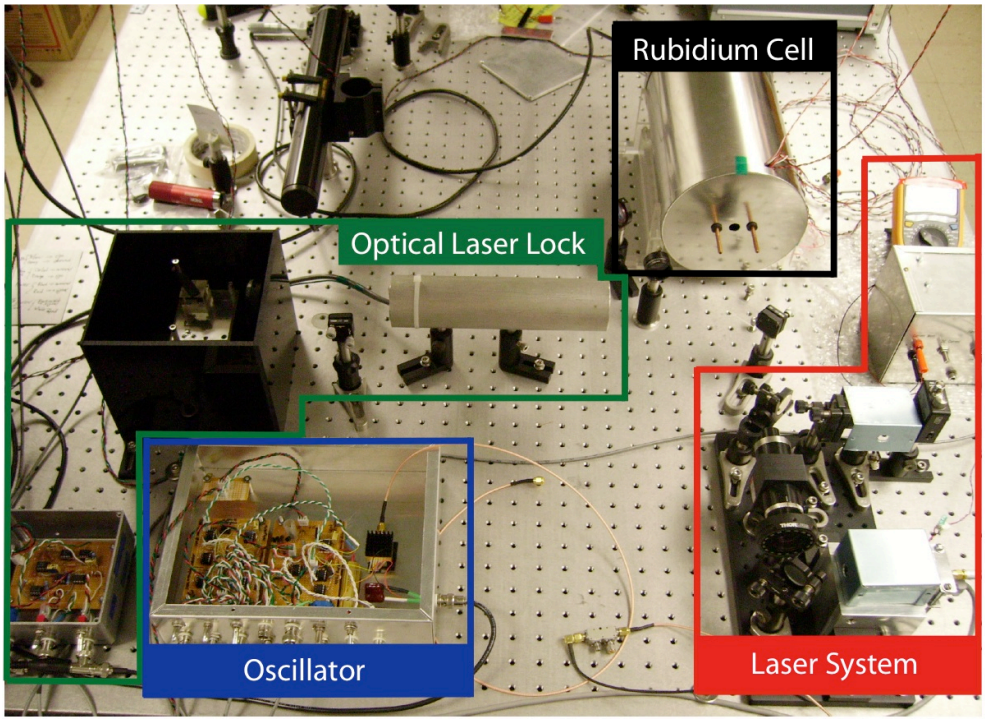

Figure 3: Layout of the experiment on the optical table. Laser system is in the red box, rubidium cell and shields in the black box, DAVLL in the green box, and oscillator in the blue box.

create a clock and study coherent population trapping. In this section, each part will be explained, showing how the system as a whole comes together to create the clock and study CPT.

3.1 Laser

Since this is an original project, we had complete control over the design and fabrication of the hardware for the laser system. Using ideas from Sergey Zibrov at the Lebedev Physics Institute in Russia, who had designed a temperature controlled diode laser system, a system was created that would be robust yet easily assembled and disassembled when changing laser diodes. The laser needed to be held at a fixed temperature to achieve stability in wavelength, so the system was designed to keep the laser at a given temperature.

Figure 4 shows the laser system designed by our group. The system provides the laser with a stable temperature and modulation of the laser's current, which are both necessary in the prototype atomic clock. The basis for the laser system is the heat sink, which doubles as the holding block for the system. The temperature controller uses a peltier, which is a thermo-electric heater and cooler, and maintains a stable temperature of the laser. A copper block containing a collimating lens and the laser is then placed on the peltier. The SMA on the laser is connected to a Bias-T, which mixes rf modulation and dc current and outputs to the laser. The rf signal is input

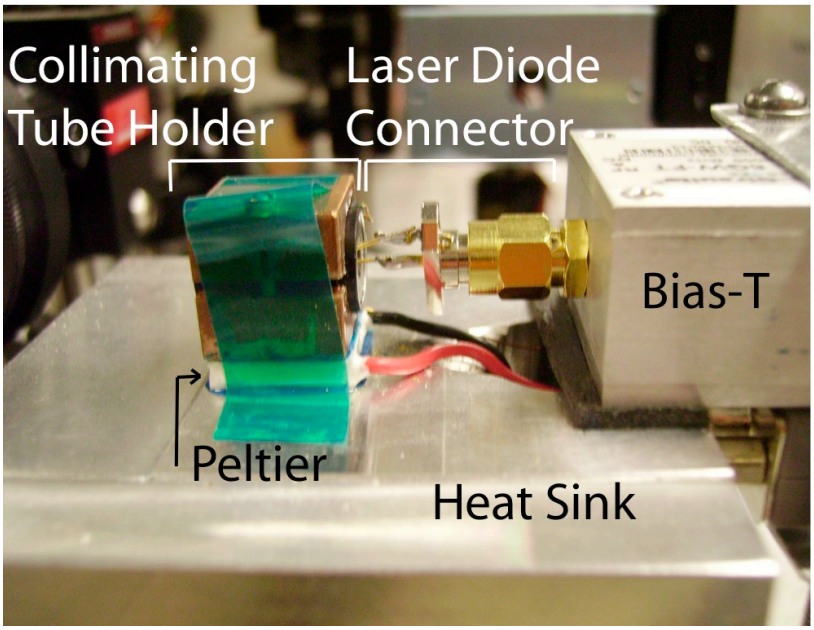

Figure 4: The laser system.

to the Bias-T by a modulator, and the dc current is provided by a constant current source.

To stabilize theair temperature around the laser, we use a metal box with a hole for the laser that is placed on top of the heat sink and around the collimating tube holder. This stabilizes the air around the laser, because the small airflow in the laboratory is enough to cause temperature fluctuations large enough to affect the wavelength of the laser. Changes in the wavelength of the laser are not good for the stability of the clock, and may be one factor that affects how long the clock stays locked.

The laser of choice is a vertical-cavity surface-emitting laser (VCSEL), which has useful characteristics for this application: low power consumption and ease of current modulation with rf signals. The VCSEL has a maximum current of 2 mA, which requires a very low current source that does not add much noise to the current. Much of the research done last summer was to find a power supply for the laser that could operate within these constraints. The laser's ability to maintain a constant frequency in the range needed to remain on a rubidium resonance is very much determined by the ability of the power supply to maintain a constant current. After trying one commercial power supply and two designs of power supplies of our own, one design was found to operate with stable constant current and little noise. Using four D-cell batteries to power the constant current source and the circuit in figure 5 to maintain a constant current, a power supply was fabricated that suits the needs of the laser. For a further analysis of the issues associated with the power supplies, refer to [1].

There are two factors that influence the laser's frequency, both of which are in our control. One is the temperature, which is controlled by the peltier and driven by a temperature controller, and the other is input current, which is controlled by the

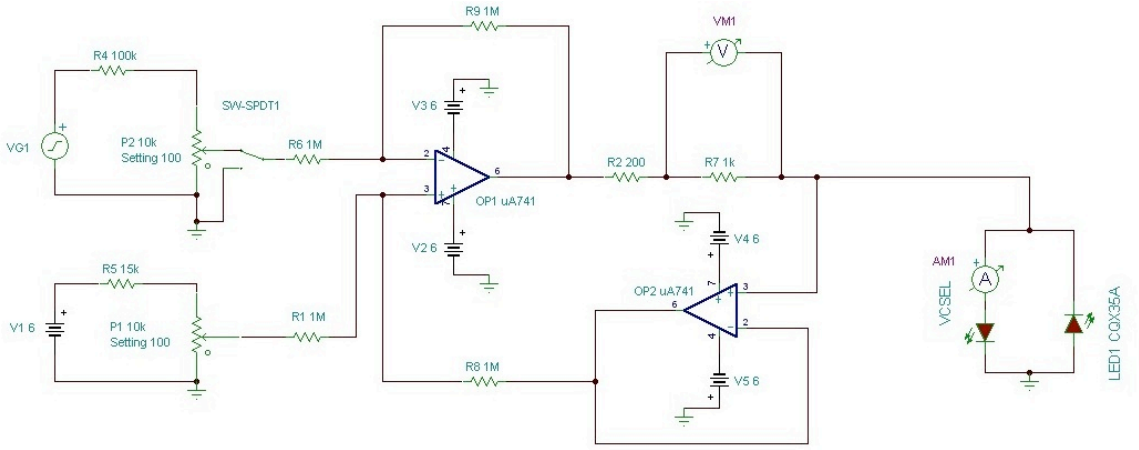

Figure 5: The schematic for the battery-powered constant current supply of the laser.

constant current source. Increasing either the temperature or the current increases the laser's frequency, so we must balance these two to keep the laser at an absorption resonance frequency. Since there was incentive to increase the laser's current (more modulation power), the temperature had to be lowered to keep the laser on resonance. After finding the operational conditions to have a current of approximately 1.35 mA and a temperature of 29.02 degrees C, the CPT and clock measurements were taken.

3.2 VCSEL Modulation

After the VCSEL was installed in the laser system, measurements were taken to see modulation of the laser. The experimental setup and results are given below.

To see signal that has meaning for phase modulation, an interferometer (Fabry-Perot cavity) must be used. A Fabry-Perot cavity is a set of two mirrors with 99 percent reflectivity aligned such that the mirrors are parallel with each other and perpindicular with the beam (see figure 6). When this alignment is achieved, the waves reflecting off the mirrors constructively interfere to create transmission through the mirrors at frequencies separated by the free spectral range (FSR). The FSR is the frequency spacing of the cavity's axial resonator modes, and is given by the equation:

$$\Delta\nu = \frac{c}{2L} \tag{30}$$

where L is the distance between mirrors. For the early measurements of VCSEL modulation, a purchased Fabry-Perot cavity with length of 5 cm and FSR of 1.5 GHz was used. This FSR was not enough to resolve the rf modulation comb, so a cavity with a length of approximately 5 mm was created from two mirrors. We achieved an FSR of approximately 40 GHz and a finesse of approximately 100, which allowed resolution of second and third modulation sidebands at 6.8 GHz.

This Fabry-Perot cavity was fabricated by epoxying two piezoelectric crystals on a lens mount (see figure 6; the piezos are the green pieces on the top mirror) and connecting their wires to a BNC connector. Piezoelectric crystals work by changing

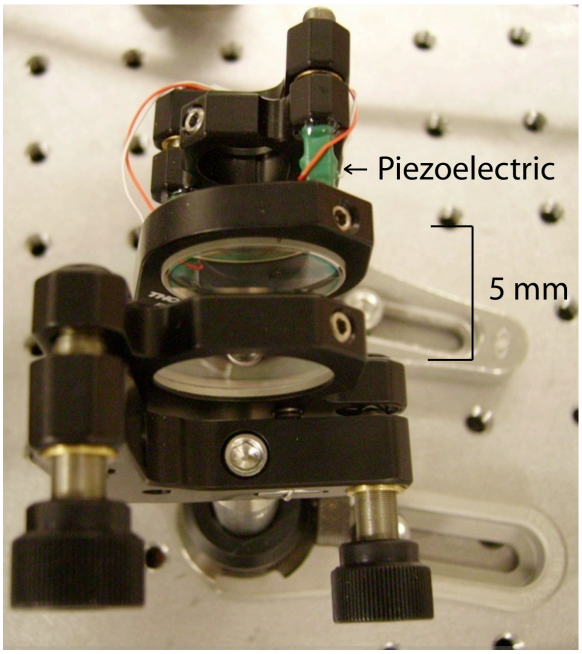

Figure 6: The Fabry-Perot cavity with length of approximately 5 mm.

the length of the crystaline structure in one plane based on the input voltage, and the BNC connector was attached to a piezo scanner (made by ThorLabs), which provided an input voltage. The piezo scanner was modulated with a function generator to provide scanning of the length of the cavity, providing transmission of the wave through the cavity and giving a signal on the oscilloscope.

Alignment of the Fabry-Perot cavity has proven difficult with the low powered lasers, because of the decrease in signal after the cavity. To align the cavity, an iris is placed after the optical isolator (see figure 7) to indicate the position of the reflection. The mirror with the piezoelectric crystals (see figure 6) is installed on the optical table, and its reflection is moved with screws on the optical mount to be directly back into the iris. The front mirror is then installed, and its reflection is also moved back into the iris. Both mirrors' reflections are moved into the iris to crudely align the mirrors to each other and to the incident beam, and then fine-tuned to each other and the photodetector with the screws on the mirror mounts.

For the modulation measurement, either the Fabry-Perot cavity or the current into the laser could be scanned. Using the optical setup in figure 7, the modulation figures for both the Modulation Synthesizer and the Stellex Mini-YIG were taken by scanning the Fabry-Perot cavity.

To create the carrier and sideband comb needed in the experiment, the current of the laser must be modulated. There are two sources of rf modulation: one using a commercial digital synthesizer (Agilent E8257D); and the other using a Stellex Mini-YIG Oscillator (refer to figure 8). The commercial digital synthesizer produces modulation at very precise frequencies up to 14 dBm, and figures 9-11 were taken with this modulation source. We observed various sideband-to-carrier ratios according to the input power, and achieved very close to a 1-to-1 sideband-to-carrier ratio at 14

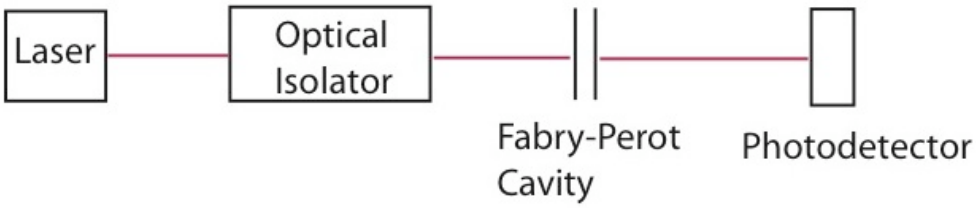

Figure 7: Visual schematic of optical setup for measurement of phase modulation.

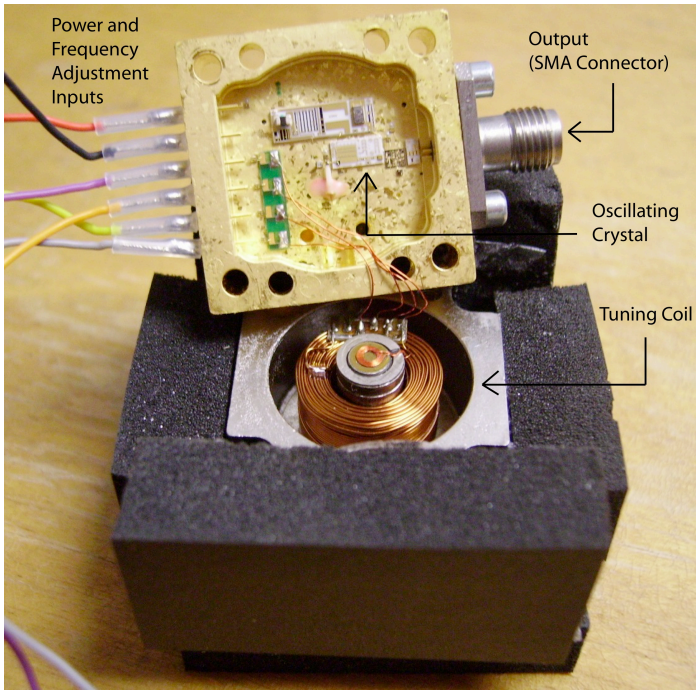

Figure 8: The inside of the Stellex Mini-YIG oscillator. Changing the current in the coil changes the frequency of the output modulation.

dBm (figures 9-11). When connected to the Stellex, we achieved sidebands greater than the carrier for 15 dBm input power and approximately half of the carrier for 14 dBm input power (figures 12, 13). The data was taken with the short Fabry-Perot cavity (figure 6) while sweeping the piezoelectrics.

To demonstrate improving oscillator stability by locking it to the atomic resonance, we also purchased a tunable Stellex crystal oscillator. This oscillator uses a crystal to generate modulation between 5.95 and 7.15 GHz at approximately 15 dBm of power. The modulation frequency can be changed by increasing or decreasing the current in a tuning coil, which changes the magnetic field strength on the crystal. Because of the inductive nature of a tuning mechanism, it turned out to be important to use a constant current source, rather than a commerical function generator (which provides constant voltage). In fact, two function generators were damaged in

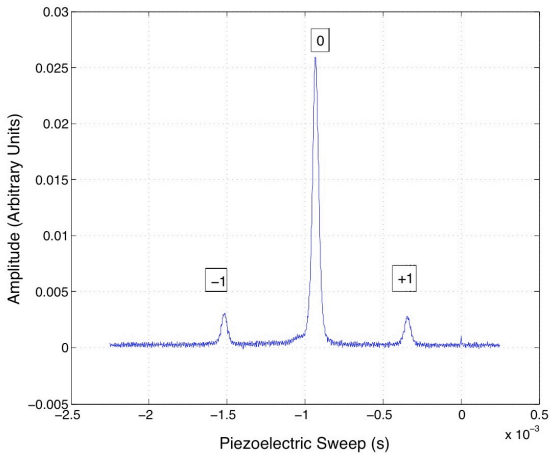

Figure 9: Modulation with the Agilent E8257D at 6.8 GHz and 5 dBm of power.

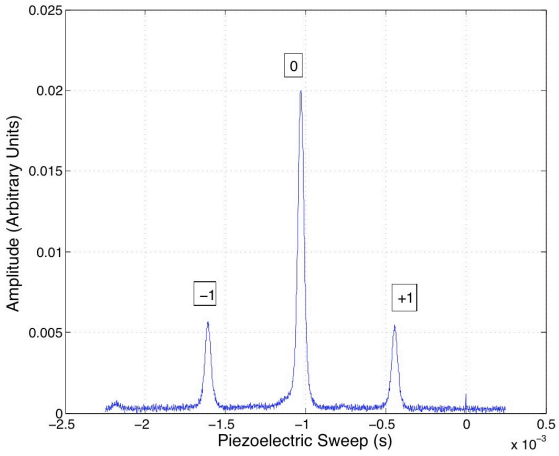

Figure 10: Modulation with the Agilent E8257D at 6.8 GHz and 9 dBm of power.

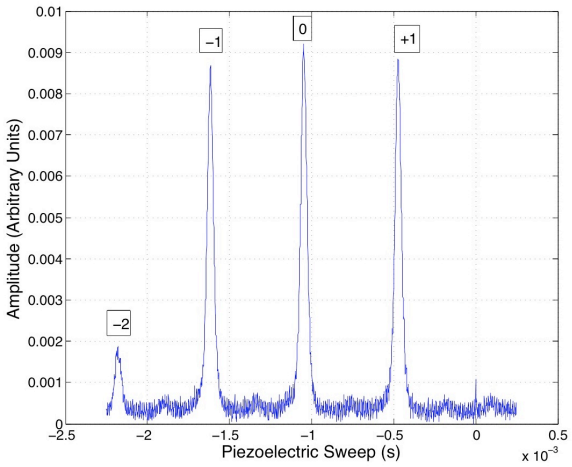

Figure 11: Modulation with the Agilent E8257D at 6.8 GHz and 14 dBm of power.

the process of testing the oscillator.

After understanding the need for a constant current source, one was designed and fabricated. The calibration of the Stellex with input current to modulation frequency is seen in figure 14. We have found a 100 MHz increase in frequency for every 20 mA increase in current, and modulation at 6.834 GHz requires 140.3 mA. There is also the ability to modulate the frequency of the Stellex at low frequencies by connecting an external function generator, and we have limited the range of low frequency modulation to 1.5 MHz. For reference, figures 12 and 13 were taken with the Stellex modulation.

One interesting result found centered on the "saturation" of the signal on the oscilloscope based on the modulation power and current. Saturation of the signal occurred when there were too many sidebands with not enough energy in each, causing a drop of the signal from sharp, high peaks to wide, low peaks barely above the noise

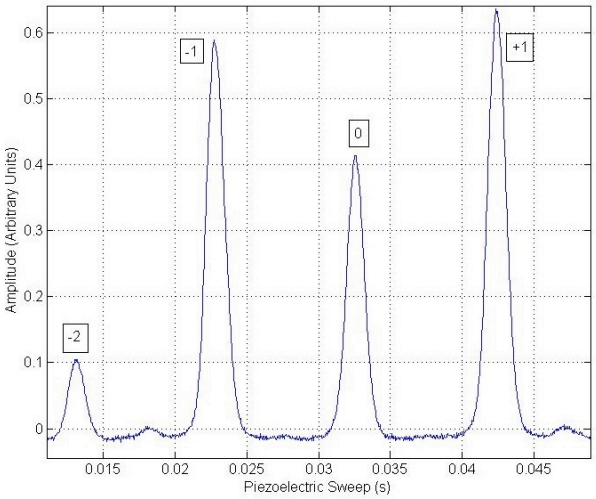

Figure 12: Modulation with the Stellex with 15 dBm input power.

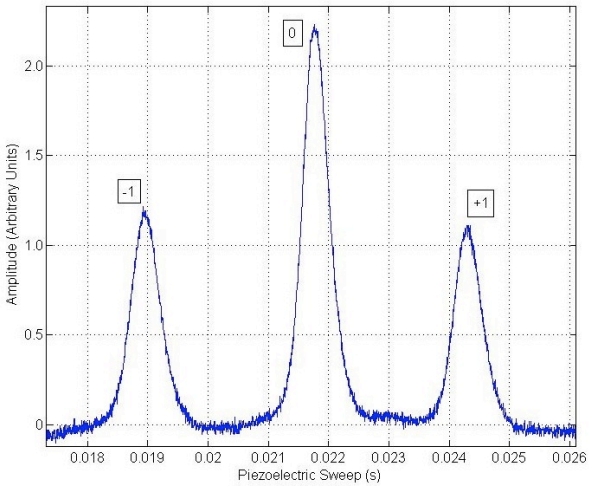

Figure 13: Modulation with the Stellex with 14 dBm input power.

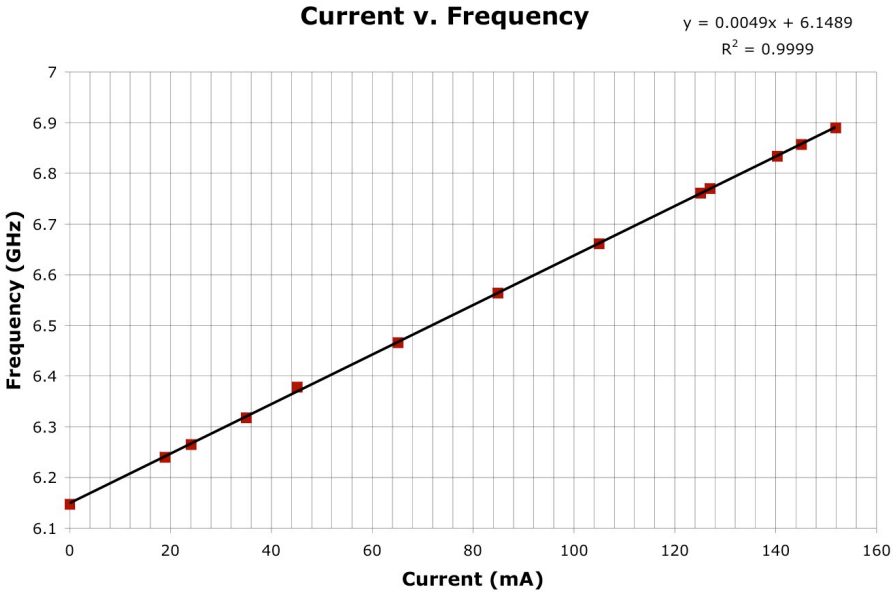

Figure 14: Calibration of the Stellex Mini-YIG oscillator.

on the scope. We found that the saturation depended on the input current, meaning low current with high modulation power gave saturation of the sideband-carrier comb. We also found that the VCSEL could modulate at higher powers when lasing with higher currents, so the current was increased.

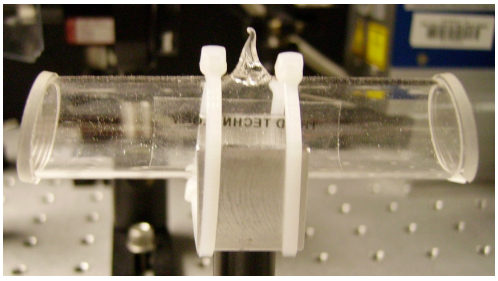

Figure 15: Rubidium vapor cell. Contains a gaseous rubidium with neon as a buffer gas.

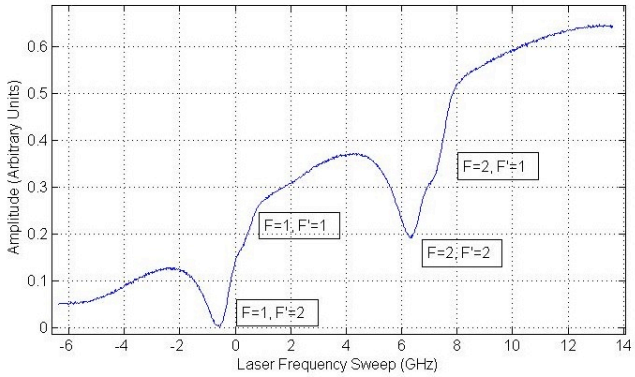

Figure 16: Rubidium resonances seen in an isotopically pure ^{87}Rb cell.

3.3 Rubidium Cell, Solenoid, and Shields

Another main component of the experimental setup is the rubidium cell. We have two cells in our system; one is encased in magnetic shields and a solenoid and used in CPT and creating the clock, and the other is in our optical locking system to maintain the correct optical frequency. The next section is devoted to the optical locking system, so here we will descibe the purpose of the cell in the shields and solenoid. The cells are identical to the one in figure 15, and come in two varieties: one with natural abundantly mixed ^{87}Rb and ^{85}Rb; the other with isotopically pure ^{87}Rb. The cell in the shields and solenoid is isotopically pure ^{87}Rb, and is also filled with neon to act as a buffer gas. Because gas has a high velocity and freedom to move in any direction, the atoms have many collisions with the cell walls per unit time. When a rubidium atom in the dark state collides with a wall, it loses the dark state and decays into a ground state. This is not good for the experiment, because we want the atoms to retain their dark state for the maximum amount of time. A buffer gas relieves this problem by reducing the number of rubidium atom collision with the walls, and also conserves the spin of the rubidium atoms when it collides with the rubidium. There exists an optimal buffer gas pressure in the vapor cell, which is determined by many different experiemental parameters [3] and needs to be calibrated for this experiment.

Any nonhomogeneous magnetic field splits magnetic levels and affects the EIT. To avoid stray fields from the laboratory environment, the rubidium cell is placed inside a set of three cylindrical magnetic shields. When needed, we separate the Zeeman energy levels of the ground state by creating a weak homogeneous magnetic field. This magnetic field is made by surrounding an isotopically pure ^{87}Rb cell with a solenoid, which has a main coil in the middle and two small correction coils on either end. This solenoid is covered with an inner shield, which is wrapped with a resistive wire connected to a temperature controller. All of these parts are then covered with insulating foam, and placed inside the middle shield. The middle shield is also covered with insulating foam, and placed inside the outer shield (see figure 17). The shields limit the influence of external magnetic fields on the vapor cell, allowing more precise control of the frequency of the hyperfine spacing. After assembly, the shields are

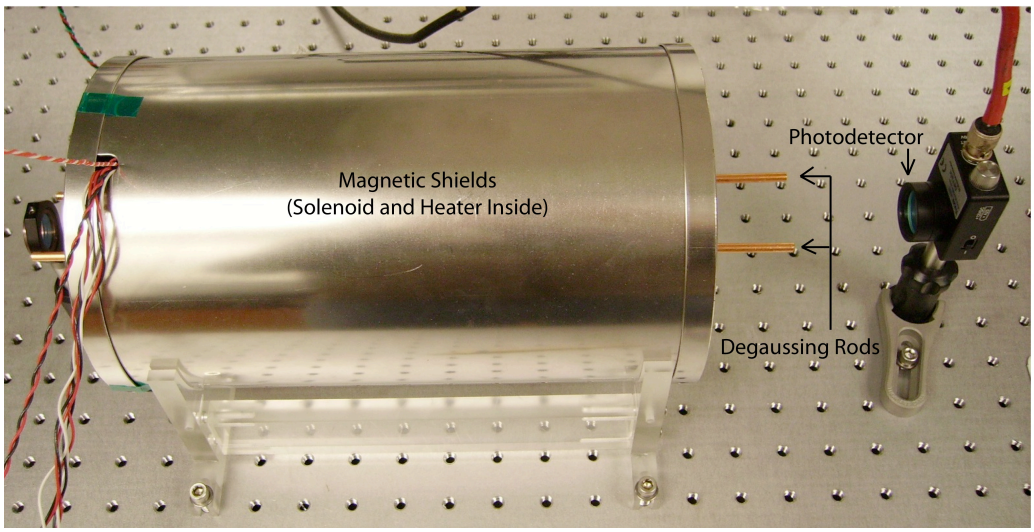

Figure 17: Outer shield, with two more shields, a solenoid, and the rubidium cell inside.

degaussed by running a large current through each degaussing rod. The shields are then aligned in the beam path, and become part of the experimental setup.

3.4 DAVLL

The DAVLL system plays an important role in the prototype atomic clock because it allows locking of the frequency of the VCSEL to a specific resonance of rubidium. Utilizing a feedback system that monitors the current of the laser (see figure 18), DAVLL keeps the lasing frequency equal to the rubidium resonance frequency. The DAVLL consists of two parts: an optical part containing a natural isotope rubidium vapor cell, half and quarter waveplates, linear polarizing plate, two perpendicularly aligned balanced photodiodes, and a small differentiating circuit (see figure 21); and an electronic part consisting of a fairly complicated circuit. The optical part produces the raw differential signal (also known as an error signal, (d) in figures 19 and 20) that is input to the electronics, and the electronics creates the feedback necessary to maintain the laser's frequency.

3.4.1 Optics

The optical part of the DAVLL is shown in figure 21. To lock the laser frequency we split part of the laser beam and pass it through the natural abundance rubidium cell inside the strong (50 G) homogeneous magnetic field. Linear polarization of the light is ensured by the polarizing plate before the cell, and the relative polarization direction is controlled by the half waveplate. Because of the strong magnetic field, the resonance absoprtion lines for two circularly polarized components of the laser field are shifted in opposite directions from its original position due to the Zeeman shift (as seen in figures 19 and 20). Each photodiode is aligned according to a procedure,

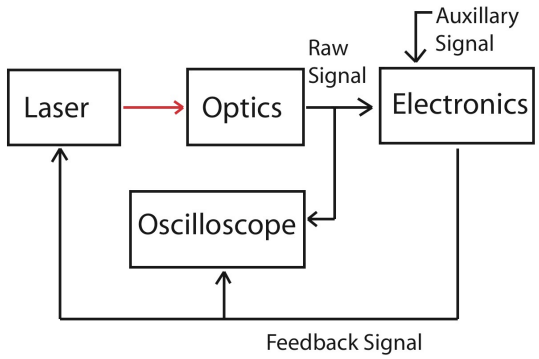

Figure 18: Flow chart of DAVLL operation.

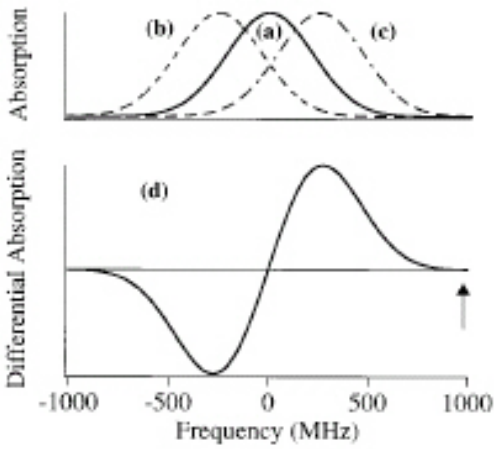

Figure 19: Absorption and differential spectra from the DAVLL system. (a) represents unshifted absorption, while (b) and (c) represent the hyperfine shifted absorption resonances. (d) is the differential of (b) and (c).

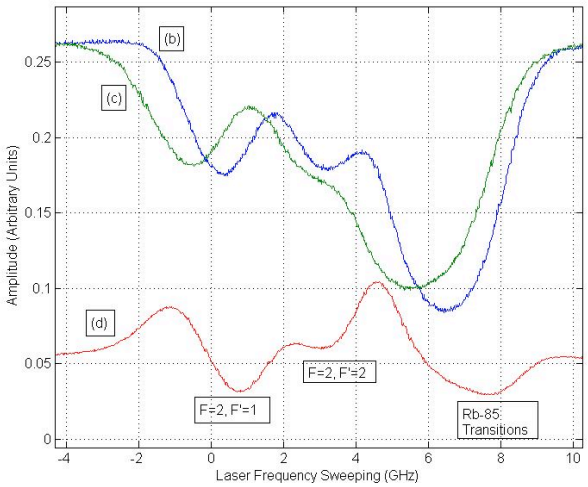

Figure 20: Experimental absorption and differential data taken from the DAVLL. (b) and (c) are the hyperfine shifted absorption resonances, and (d) is the differential of (b) and (c).

and their waveforms are subtracted to give the error signal seen in part (d) of figures 19 and 20. The data collected by our group of each photodiode and their differentials are seen in figure 20. This differential signal is then sent to the electronics as the Raw Signal (see figure 18), where it is fed back to the laser.

3.4.2 Electronics

The second part of the DAVLL system is the electronics. Its responsibility is to maintain a constant laser frequency by amplifying the raw signal from the optics and adjusting the laser current accordingly. The raw signal represents an error signal, and the steep antisymmetric nature of the signal (see part (d) in figure 19) acts as a

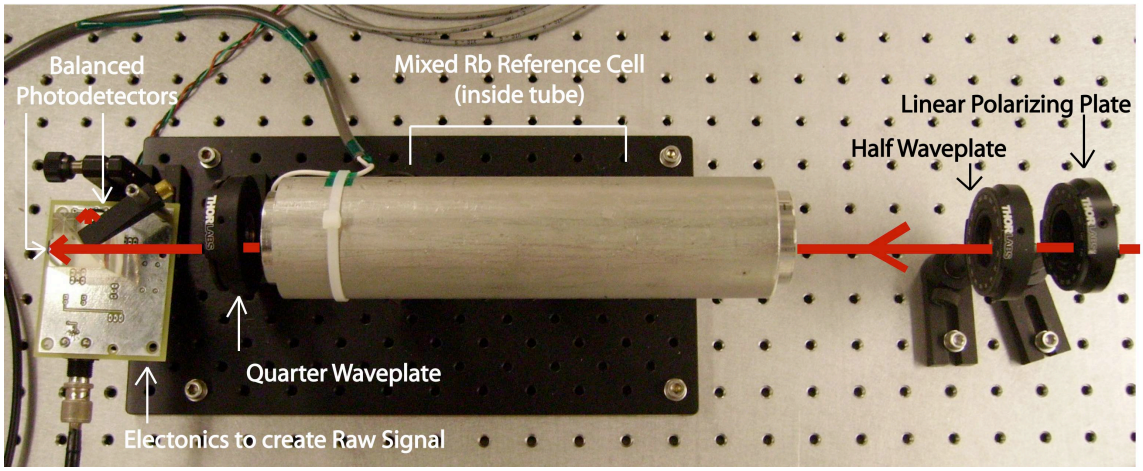

Figure 21: The optical hardware of the DAVLL system. The full hardware includes the optical hardware plus a circuit that provide the feedback to the laser.

guide to increase or decrease the current to the laser. As an example, if the frequency read by the photodetectors is higher than the zero point, the electronics will supply less current to the laser so that the laser's frequency will decrease. When the laser's frequency is lower than the zero point, the electronics will supply more current to the laser to increase its frequency. This process should continue indefinitely to keep the laser's frequency resonant with desired optical transition in the isotopically pure vapor cell.

Unfortunately, there is a small offset in the raw signal from the optics. This offset in the raw signal causes tension between the raw signal and feedback to the laser. The feedback should have small continual fluctuations around the zero point, but the offset in the error signal drives the feedback to fluctuate around a non-zero point. This causes us to question whether the laser is locked on resonance or if the two signals are not physically representative of the locking. A part of the optical system that causes the offset is the quarter waveplate. As the temperature of the glass changes, so does the phase of the laser passing through. To alleviate this problem, we have moved the quarter waveplate and balanced photodetectors into a box with a heater. This provides a constant temperature for the quarter waveplate, and has decreased the offset issue.

Until now, nothing has been said about the Auxiliary Signal in figure 18 (same signal as Aux Input in figure 22). This signal is designed to help us initially find the correct current range the laser needs to lock with rubidium resonance in the isotopically pure vapor cell and serve as a check when we believe the laser is not locked. The problem with the Aux Input is that the voltage scale from a function generator is variable from approximately 100 mV to 20 V, while the raw signal's voltage does not exceed more than approximately 100 mV. Because of this large discrepancy in voltage, several changes have been made to the DAVLL electronic circuit to allow the two inputs to be on the same voltage scale. These changes have been tested and work completely. When the laser is optically locked, the Aux signal

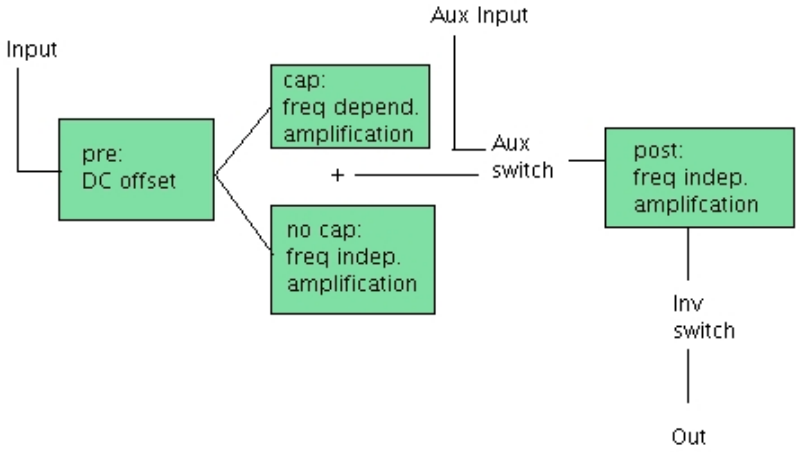

Figure 22: Flow chart of DAVLL electronics operation. The words pre, cap, no cap, and post refer to potentiometers in the circuit.

is not needed anymore, and ignored until the system comes out of lock.

4 CPT Experimental Results

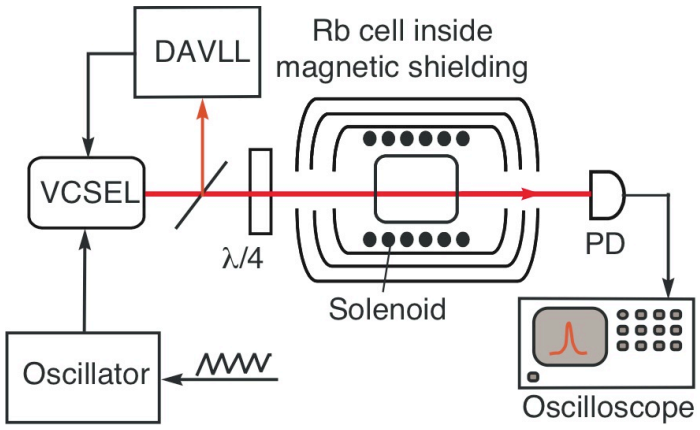

Figure 23: Setup schematic for the CPT experiment.

As a part of the clock, we need to create a coherent population trapping (CPT) peak that will serve as our reference signal. To do this, we follow the schematic in figure 23. The laser is first phase modulated at the same frequency as the hyperfine splitting of the ground states (6.834 GHz), and then sent through the rubidium cell and into a photodetector. The laser is split before the rubidium cell and also sent to the DAVLL system, which locks the laser to the optical frequency between the ground and excited states. We read the signal from the photodetector on an oscilloscope, and record the signal from the oscilloscope with a LabView program.

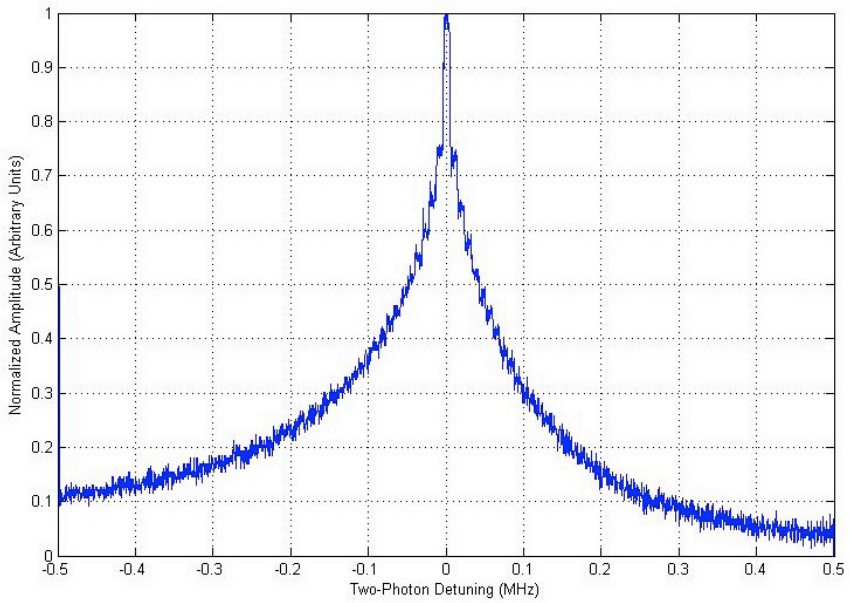

Figure 24: Single CPT peak with 1 MHz slow modulation sweep of the phase modulation.

Figure 24 is an example of a signal that is seen on the oscilloscope when we have achieved CPT. When the frequency of the phase modulation matches the hyperfine splitting frequency and the optical frequency is locked by the DAVLL system, the atoms are in a dark state and we see transmission of the laser through the rubidium cell. The laser is swept with an added modulation (1 MHz in figure 24) through the central frequency, so we can see detuning from dark state.

We also performed studies on the effect of laser power on the shape of the CPT resonance, and the results are seen in figures 25, 26, and 27. To reduce the power, we placed neutral density (ND) filters in front of the rubidium cell so that less laser light would enter the cell. We then sent the signal from the photodetector to the oscilloscope, and recorded the data with the computer. For the 500 kHz sweep, we see a difference in the lineshape when the laser power is reduced from .1 ND filter to .3 ND filter, but not from .3 ND filter to .5 ND filter. For the 50 kHz sweep, there is a difference in lineshape for all three powers. Lastly, there is no difference in the lineshapes for the 5 kHz sweep.

These results are consistent with the widths predicted by equation (25)

$$\gamma_{CPT} = 2\Gamma_{dark} + \frac{\Omega^2}{\Gamma}, \tag{31}$$

because as the intensity of the field increases (related through Ω), the width of the resonance increases. We see this in the 500 kHz sweep and 50 kHz figures, but not in the 5 kHz sweep figure. We do not see the increase in the width in the 5 kHz figure because this sweep only shows the very top of the resonance, and has its shape predicted by a different equation.

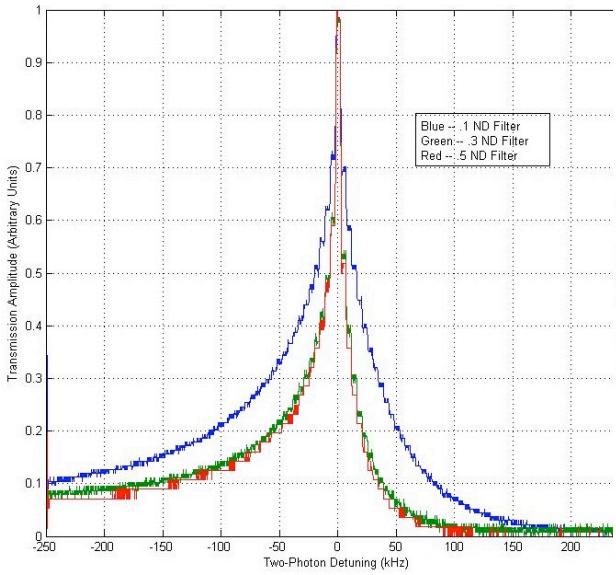

Figure 25: Changes in the lineshape of the CPT resonance for changing laser power. The two-photon detuning is 500 kHz.

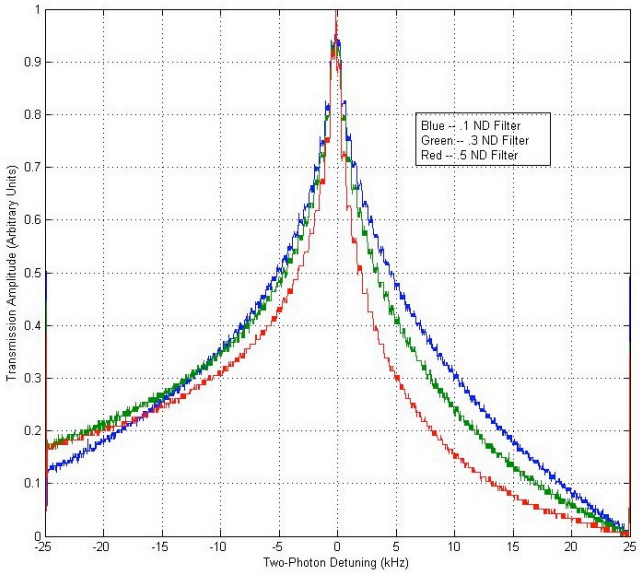

Figure 26: Changes in the lineshape of the CPT resonance for changing laser power. The two-photon detuning is 50 kHz.

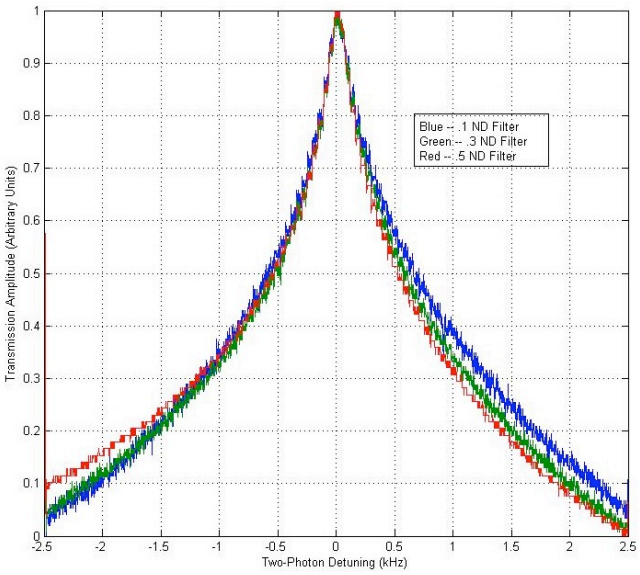

Figure 27: Changes in the lineshape of the CPT resonance for changing laser power. The two-photon detuning is 5 kHz.

5 Clock Experimental Results

To create the clock, we take the CPT setup and add a few parts (refer to figure 28). Again, the laser is phase modulated at the same frequency as the hyperfine splitting of the ground states (6.834 GHz), but the modulation is set with a PID controller. Slow frequency modulation is added to the modulation from the PID controller and also

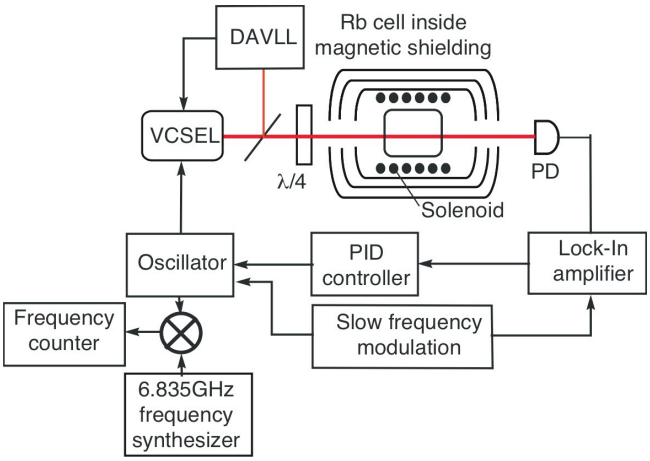

Figure 28: The clock experimental setup.

sent to a lock-in amplifier, which acts a narrow bandpass filter to provide a feedback signal for the PID controller. The laser is again split before the rubidium cell and also sent to the DAVLL system, which locks the laser to the optical frequency between the ground and excited states. The signal from the oscillator (a combination of slow frequency modulation and modulation at the hyperfine splitting frequency) is sent to a mixer, which also takes in a signal from a stable reference frequency. The two signals are beaten together, and analyzed by a frequency counter. The frequency of the beats determines the accuracy of the clock, which is given in a form known as the Allan variance.

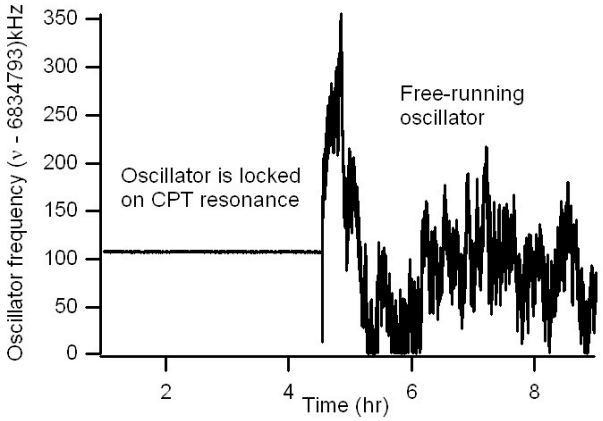

Figure 29: The oscillator when optical and rf locked versus free-running.

In figure 29, we can see a significant difference in oscillator frequency when the PID controller is locked versus free-running. For the free-running case, the oscillator changes frequency by ±175 kHz; the locked oscillator only changes frequency by ±100 Hz. Through many improvements in the PID controller electronics, using a more accurate counter and reference frequency, temperature stabilizing the DAVLL photodetectors and quarter waveplate, changing the rubidium resonance locking point,

and improving the signal to the lock-in amplifier, the oscillator now changes frequency by ±2 Hz when locked. These changes in frequency correspond to an Allan variance [8], which is given by the equation

$$\sigma_\nu^2(\tau) = \frac{1}{2}\left\langle \nu^2 \right\rangle \tag{32}$$

This equation says that for each time interval τ, the expectation value of ν is calculated. The variable ν is the difference in the measures of each succesive frequency; *i.e.* if i denotes the ith measurement of ν, then $\nu = (\nu_i + 1) - \nu_i$. Each adjacent difference of ν is then squared and averaged over a given time period, and finally divided by two. The divide by two causes this variance to be equal to the classical variance if the data is taken from a random and uncorrelated set (also known as white noise). In addition, Allan variance is a unitless quantity.

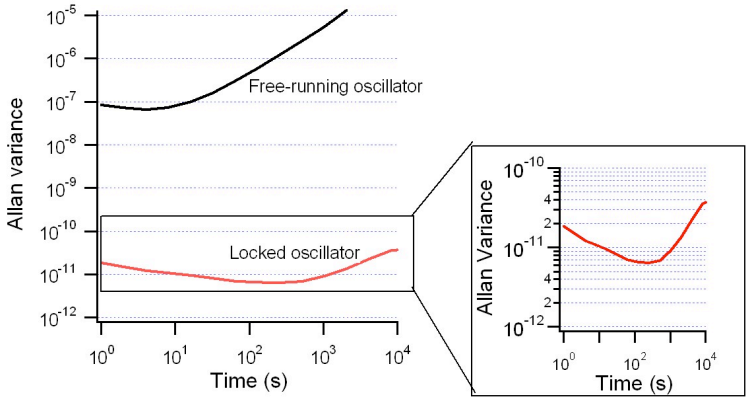

Figure 30: Allan variance with the clock locked (red) and free-running (black).

Again we compare the free-running oscillator versus the locked oscillator, this time using an Allan variance plot. The corresponding Allan variance for the ±175 kHz case is 9×10^{-8} over a time period of 10 seconds, while the ±2 Hz case corresponds to 8×10^{-12} over 100 seconds. To put this into perspective, if we could lock our clock at an accuracy of 8×10^{-12} for a long enough time period, we would lose 1 second every 4000 years. The standard cutoff for whether or not a clock is even considered is 10^{-11}, so we are pleased that we have achieved this result. In addition to measuring the accuracy of the clock, we also measure how long the clock stays optically and rf locked. Our best attempt yielded a locking time of 41 hours with a 6 Hz drift, which is good considering the poor quality of our oscillator.

There has been a very large improvement in the performance of the clock, and this has come from various changes in clock system. One area of improvement has come from finding the best point to use the lock-in amplifier. The lock-in amplifier produces a steep anti-symmetric curve (like the DAVLL differential signal), and we wanted to find the modulation depth and modulation frequency that would produce the largest slope. We changed the modulation depth and modulation frequency, and found values for each combination. These values were then compiled into the figure 31

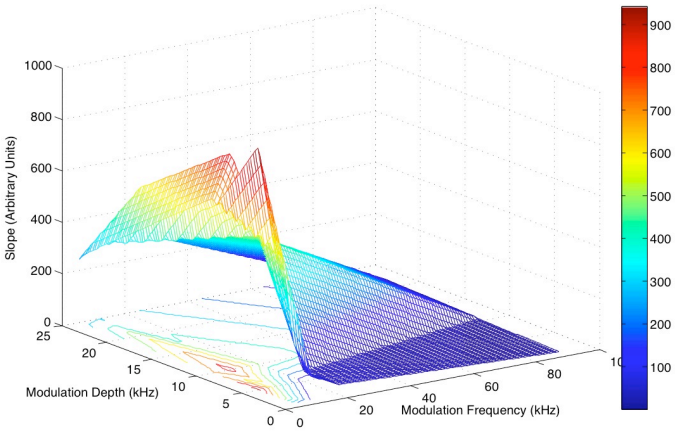

Figure 31: Modulation depth (y-axis), modulation frequency (x-axis), and slope (z-axis) plot.

and used to find the best locking point. The optimal locking condition was at 5 kHz modulation frequency and 5 kHz modulation depth. Another area of improvement has come in modifying the circuits that form the PID controller. This controller is responsible for the frequency of oscillation produced by the modulator, and improving the frequency drift of the electronics has improved the stability of the oscillator. We have also learned how to lock the DAVLL such that the optical locking is more stable, giving us a longer time in which the clock is locked. Another area of improvement is in the hardware. We have purchased a more stable lock-in amplifier, counter, and reference frequency, and these upgrades have given improvements in the Allan variance. In addition, we have temperature stabilized the DAVLL photodectors and quarter waveplate and the rubidium cell in the shields, and this has led to another improvement in the Allan variance.

6 Further CPT Studies

While creating the clock was good and necessary, the real focus of this experiment is to improve the CPT. To understand and further develop knowledge about CPT, we must begin studying the underlying physics of the effect. For future work, we will use the transition from F = 2 to F' = 1 (instead of F = 1 to F' = 2) driven by two parallel linearly polarized electromagnetic fields (instead of two circularly polarized fields). We will check the effect on reducing laser power on the lineshapes of the CPT, study the effect of an applied magnetic field, and perform other tests with the system. As usual, much work has been done, but more work is still waiting.

7 Conclusion

Through construction of the experimental system, we have seen coherent population trapping and created a prototype atomic clock. We have achieved a short-term stability of 8×10^{-12}, and have locked the clock for 41 hours with a 6 Hz drift. Work will continue on characterizing and optimizing the CPT resonances, to improve short-term and long-term stability and understand the underlying physical mechanisms of this effect.

8 Acknowledgements

I would like to thank Irina Novikova for allowing me to work on this project, and Eugeniy Mikhailov for all of his help with the project. Also to Sergey Zibrov for his ideas on the laser setup, Nate Philips for answering general lab questions, Chris Carlin for his excellent work on the DAVLL hardware system, and Jonny, Paul, and Jeb for reading this manuscript.

References

[1] N. Belcher and I. Novikova. *VCSEL Laser System for Atomic Clocks.* The College of William and Mary REU Report. August 2007.

[2] D.K. Serkland, et al. *VCSELs for Atomic Clocks.* Proceedings of the SPIE, Volume 6132, pp. 66-76. 2007.

[3] S. Brandt, et al. *Buffer-gas-induced linewidth reduction of coherent dark resonances to below 50 Hz.* Physical Review A, Third Series, Volume 56, Number 2. August 1997.

[4] M. O. Scully, et al. *Quantum Optics.* Cambridge University Press. New York, New York. 2002. pp. 227-228.

[5] S. Knappe, et al. *Characterization of coherent population-trapping resonances as atomic frequency references.* Journal of the Optical Society of America, Volume 18, Number 11, pp. 1545-1553. November 2001.

[6] K. W. Vogel. *Dichroic Atomic Laser Locking Setup.* University of Michigan REU Program Report. August 3, 2004.

[7] D. W. Allan, et al. *The Science of Timekeeping.* Hewlett-Packard Application Note 1289. 1997.

[8] D. W. Allan. http://www.allanstime.com/AllanVariance/. February 2004.